Light bullets in nonlinear waveguide arrays under the influence of dispersion and the Raman effect

Truong X. Tran,[1,2] Dũng C. Duong,[1] and Fabio Biancalana[2,3]
[1]*Department of Physics, Le Quy Don University, 236 Hoang Quoc Viet Street, 10000 Hanoi, Vietnam*
[2]*Max Planck Institute for the Science of Light, Günther-Scharowsky-Straße 1/Bau 24, 91058 Erlangen, Germany*
[3]*School of Engineering and Physical Sciences, Heriot-Watt University, EH14 4AS Edinburgh, Scotland, United Kingdom*
(Received 29 July 2014; published 28 August 2014)

We study the formation and the dynamics of spatially broad light bullets generated in silica waveguide arrays. We show that these bullets are metastable even in the presence of high-order dispersion, coupling dispersion, and the Raman effect and can be approximated by the hyperbolic secant function with a high degree of accuracy. We also investigate the formation of narrow light bullets which are spatially localized in only a few adjacent waveguides and short in time. We reveal that the latter are extremely robust even in the presence of the Raman effect.

DOI: 10.1103/PhysRevA.90.023857 PACS number(s): 42.65.Wi, 42.81.Dp

I. INTRODUCTION

Waveguide arrays (WAs) present a unique discrete periodic photonic system to investigate many interesting fundamental phenomena such as discrete diffraction [1,2], discrete solitons [1,3–6], high-power propagation [7], and photonic Bloch oscillations [1,8–11]. In applications, two-dimensional networks of nonlinear waveguides with discrete solitons may be useful for designing signal-processing circuits [12]. Binary WAs have also been intensively used to mimic relativistic phenomena typical of quantum field theory, such as *Zitterbewegung* [13], the Klein paradox [14], fermion pair production [15], and the Dirac equation in the linear regime [16]. Quite recently, the optical analog of relativistic Dirac solitons with exact analytical solutions in binary WAs was found in [17] and numerically proved to be very robust [18], which could potentially pave the way for using binary WAs as a classical simulator of quantum nonlinear effects arising from the Dirac equation, something that is thought to be impossible to achieve in conventional (i.e., linear) quantum field theory.

In a recent study [19] the diffractive resonant radiation (DRR)—an analog of the well-known dispersive resonant radiation in the temporal case for optical fibers [20,21]—was found when a spatial soliton in the continuous-wave (cw) regime was launched into WAs. It turns out that the DRR is a universal effect which can occur in WAs not only in the cw regime but also in the spatiotemporal case where a long pulse is used [22]. The wave-number supercontinuum generation and the compensation of the soliton self-wave-number shift by the emitted DRR have also been revealed [22]. The supercontinuum generation in both frequency and wave-number domains in WAs was numerically shown in [23].

Light bullets (LBs) refer to spatiotemporal solitary waves which can propagate without distortion in multidimensional space and time under the combined effect of diffraction, anomalous dispersion, and nonlinearity [24,25]. They have been a subject of extensive investigation in both conservative [5,26–35] and dissipative systems [36–38]. Dynamic light bullets have also been shown to exist in normal dispersion and when plasma generation is taken into account [39]. In continuous conservative media possessing Kerr nonlinearity only, LBs are not stable and a collapse takes place [5,24]. However, it has been shown that the discreteness introduced by WAs can stop the collapse [26], and thus nonlinear WAs can be a unique platform to meaningfully investigate LBs [26–34]. It is well known that in the case of one time and one space variables (often referred to as the 1+1 case) the soliton solution of the nonlinear Schrödinger equation with Kerr nonlinearity can be analytically found, but in the $1 + N$ case—with $N > 1$ representing the number of space variables—one often needs to use numerical tools to calculate the profiles of localized structures in both continuous and discrete systems [5]. In WAs much attention has been focused on LBs with narrow states where almost all energy is localized in only a few waveguides [26–31,33,34]. In WAs of circular symmetry (where arrays are arranged in a circle) a detailed classification of different stationary solutions with less than six waveguides was presented in [30]. In linearly coupled WAs (where arrays are arranged in a line) LBs with an extremely narrow state where almost all energy is localized in only one waveguide were numerically found and investigated in [26–28]. Profiles of broad LBs where the light energy is localized in more than ten waveguides of linearly coupled arrays were numerically found in [29] by solving a nonlinear eigenvalue problem. However, so far in theoretical works on LBs with Kerr nonlinearity other important effects for pulses such as the stimulated Raman scattering, wavelength dependence of the coupling coefficient between adjacent waveguides (further referred to as the coupling dispersion), and high-order dispersion (HOD) have not been considered. It is obvious that all these effects will somehow influence the LB formation and its dynamics. For instance, it is well known that the coupling dispersion is large because it arises from the evanescent field overlap between adjacent waveguides. This in turn makes the discrete diffraction, i.e., beam spreading, wavelength dependent. This was demonstrated dramatically when a continuum generated via a microstructure fiber was injected into a single waveguide and the spectrum of the colors in the light beam was spatially dispersed at the output of the WA made of $LiNbO_3$ crystal with defocusing nonlinearity [40] (see also [23]).

In this paper we first present the generalized coupled-mode equations (GCMEs) governing the spatiotemporal effects in linearly coupled WAs made of silica, which take into account the coupling dispersion, the Raman effect, and HOD. We then investigate the generation of broad LBs and their

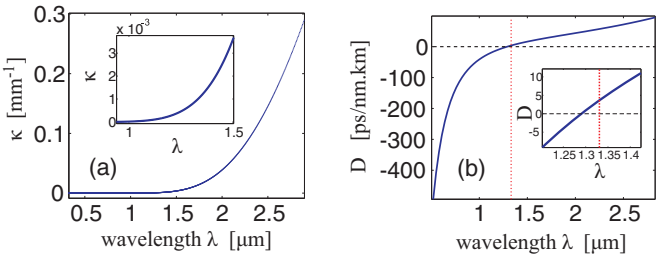

FIG. 1. (Color online) (a) Coupling coefficient κ as a function of the wavelength. Inset in (a): Zoomed version of (a) in the region of shorter wavelengths. (b) The solid (blue) curve represents the dispersion parameter D of each individual waveguide as a function of the wavelength, whereas the dotted (red) vertical line indicates the position of the cutoff wavelength at 1.3308 μm. Inset in (b): Zoomed version of (b) in the region around the cutoff wavelength. The parameters of the WA are given in the text.

dynamics during propagation. We demonstrate that these LBs are metastable and can propagate without change for hundreds of dispersion lengths even in the presence of the coupling dispersion, the Raman effect, and HOD. We show that the profiles of these broad LBs can be approximated with a high degree of accuracy by the hyperbolic secant function. We also study the formation and dynamics of narrow LBs and show that they are extremely robust even under strong disturbances of input conditions and the Raman effect.

II. GENERALIZED COUPLED-MODE EQUATIONS

Our starting point is the generalized coupled-mode equations of WAs consisting of identical waveguides made of silica in the time domain (see [23] for more details):

$$i\partial_z A_n + D(i\partial_T)A_n + \kappa(i\partial_T)[A_{n+1}+A_{n-1}] + \gamma\left(1+\frac{i}{\omega_0}\partial_T\right) \times A_n(z,T)\int_{-\infty}^{\infty} R(t')|A_n(z,T-t')|^2 dt' = 0, \quad (1)$$

where A_n is the electric-field envelope in the nth waveguide, z is the longitudinal coordinate, $T = t - z/v_g$ is the delay in the comoving frame, v_g is the group velocity at the carrier frequency ω_0, t is the time variable, the linear dispersion operator is given by $D(i\partial_T) \equiv \frac{s|\beta_2|}{2}\partial_T^2 + \sum_{m\geqslant 3}\frac{\beta_m}{m!}[i\partial_T]^m$ with $s = +1$ ($s = -1$) for the anomalous (normal) group velocity dispersion (GVD) regime, and β_m is the mth-order GVD coefficient. Note that the group velocity $v_g = 1/\beta_1$. Similarly, the operator for the coupling coefficient κ is given by $\kappa(i\partial_T) \equiv \sum_{m\geqslant 0}\frac{\kappa_m}{m!}[i\partial_T]^m$ and κ_m is the mth-order derivative of $\kappa(\omega)$ at the carrier frequency ω_0. Note that in previous works dealing with LBs in WAs the coupling dispersion has often been ignored, and thus the coupling coefficient κ has often been treated as constant, but in this specific work we would like to relax this approximation, since as shown in Fig. 1(a) the coupling coefficient strongly depends on the frequency, so this approximation is not very appropriate. Here we assume that WAs consist of identical waveguides with the nonlinear parameter of each waveguide being γ. The nonlinear response function $R(t) = (1-f_R)\delta(t) + f_R h_R(t)$, where the first term represents the instantaneous electronic contribution with $\delta(t)$ being the Dirac delta function, $h_R(t)$ is the Raman response function of the core, and f_R represents its fractional contribution. For silica, $f_R \simeq 0.18$ and the Raman effect is included through a simple model in which $h_R(t)$ has the form $h_R(t) = \frac{\tau_1^2+\tau_2^2}{\tau_1\tau_2^2}\exp(-t/\tau_2)\sin(t/\tau_1)\Theta(t)$, where $\tau_1 = 12.2$ fs, $\tau_2 = 32$ fs [41], and $\Theta(t)$ is the Heaviside step function that ensures causality. The self-steepening effect is included through the derivative ∂_T in the nonlinear terms. Now we introduce dimensionless variables $\xi = z/L_D$, $\tau = T/T_0$, and $a_n = A_n/\sqrt{P_0}$, where the dispersion length $L_D = T_0^2/|\beta_2|$ and T_0 is related to the full width at half maximum (FWHM) pulse duration in the case of a sech-shaped pulse as follows: $T_{\rm FWHM} \simeq 1.763T_0$ [41]. The power scale is $P_0 = 1/(\gamma L_D)$. With these new variables, Eq. (1) is equivalent to the following dimensionless GCMEs:

$$i\partial_\xi a_n + D(i\partial_\tau)a_n + L_D\kappa(i\partial_\tau)[a_{n+1}+a_{n-1}] + \left(1+\frac{i}{\omega_0 T_0}\partial_\tau\right)a_n\int_{-\infty}^{\infty} r(\tau')|a_n(\xi,\tau-\tau')|^2 d\tau' = 0, \quad (2)$$

where the dispersion operator now assumes the form $D(i\partial_\tau) \equiv \frac{1}{2}s\partial_\tau^2 + \sum_{m\geqslant 3}\alpha_m[i\partial_\tau]^m$, with $\alpha_m \equiv \beta_m/[m!|\beta_2|T_0^{m-2}]$, whereas the operator for the coupling dispersion now has the form $\kappa(i\partial_\tau) \equiv \sum_{m\geqslant 0}\frac{\kappa_m}{m!T_0^m}[i\partial_\tau]^m$, and the dimensionless function $r(\tau)$ is obtained by rescaling time t with T_0 in the response function $R(t)$.

Equation (2) is used later to investigate the LB generation and its dynamic in WAs. In order to simulate Eq. (2) one needs to calculate the dispersion parameter D and the coupling coefficient κ as functions of the wavelength. In the rest of this paper, as a practical example we specify the parameters for the WA as follows: the WA is formed by identical conventional step-index fibers with cladding made of fused silica and core made of silica with 1.8% dopant GeO_2. The dopant at the low concentration used here is only to ensure that the refractive index of the core (which has been well approximated with the Sellmeier equation) is slightly larger than that of the cladding. The core radius is 6 μm and the center-to-center spacing between two adjacent cores is 35.42 μm. Recent advances in femtosecond-laser writing technologies for WAs of fused silica (see [42]) make the above-proposed WA feasible.

With this specific WA one can calculate the coupling coefficient between adjacent waveguides as a function of the wavelength [43]. The obtained result is shown in Fig. 1(a). One can see that the longer the wavelength λ the larger the coupling coefficient κ. This is expected because for longer wavelengths the evanescent field spreads out more into the cladding, thus leading to an increase of the coupling coefficient. This feature of the coupling coefficient is essential in the dynamics of the supercontinuum in WAs [23,40]. The inset in Fig. 1(a) shows the zoomed version of Fig. 1(a) in the region of shorter wavelengths. The solid blue curve in Fig. 1(b) represents the dispersion parameter D of each individual waveguide as a function of the wavelength. The dispersion is anomalous ($D > 0$) when $\lambda > 1.2905$ μm and normal ($D < 0$) for shorter wavelengths. The dotted red vertical line in Fig. 1(b) indicates the position of the cutoff wavelength $\lambda_{\rm CO} = 1.3308$ μm; thus for $\lambda > \lambda_{\rm CO}$ waveguides are single mode, whereas for shorter wavelengths they are multimode. The inset in Fig. 1(b) plots

the zoomed version of Fig. 1(b) in the region around the cutoff wavelength.

III. BROAD LIGHT BULLET GENERATION AND ITS DYNAMICS IN A SIMPLIFIED MODEL

In this section we investigate the generation of broad LBs in WAs in the anomalous GVD regime where we ignore HOD, the coupling dispersion, the self-steepening effect, and the Raman effect. In this case Eq. (2) is much simplified as follows:

$$i\partial_\xi a_n + \tfrac{1}{2}\partial_\tau^2 a_n + \tfrac{1}{2}\eta[a_{n+1} + a_{n-1}] + |a_n|^2 a_n = 0, \qquad (3)$$

with $\eta = L_D\kappa(\omega_0)$. As mentioned above, this simplified model is often used to investigate LBs in WAs. In [35] the wavelength dependence of κ and HOD was considered in order to study spatiotemporal quasisolitons in arrays of silicon-on-insulator photonic wires, but the linear loss of silicon is much higher than that of silica, and one also needs to include two-photon absorption for silicon (as done in [35]); thus the nonlinearity of silicon is significantly different from that of silica used in this paper. Now we write Eq. (3) in the form

$$i\partial_\xi a_n + \tfrac{1}{2}\partial_\tau^2 a_n + \tfrac{1}{2}\eta[a_{n+1} - 2a_n + a_{n-1}] + \eta a_n + |a_n|^2 a_n = 0 \qquad (4)$$

and eliminate the linear term ηa_n through the transformation $a_n' = a_n exp(i\eta\xi)$ [see also this transformation to convert Eq. (2.5.3) into Eq. (2.5.4) in [6]], finally we get the following equation in the continuum limit:

$$i\partial_\xi a_n + \tfrac{1}{2}\partial_\tau^2 a_n + \tfrac{1}{2}\eta\partial_n^2 a_n + |a_n|^2 a_n = 0. \qquad (5)$$

Note that for the sake of making notations simple we drop the prime symbol in superscripts in Eq. (5). The above-mentioned parameters of the WA used in this work are deliberately chosen such that the dimensionless factor $\eta = 1$. However, even if $\eta \neq 1$, one can always rescale the variable $n = \sqrt{\eta}m$ in Eq. (5) such that its counterpart in the new equation is equal to unity. Therefore, in what follows the factor η will be put equal to unity. The profiles of LBs in the continuous media were numerically found in [24] based on Eq. (5), where n plays a role of a continuous spatial variable. In that case it is obvious that if $\eta = 1$ the transverse profile of LBs depends on the variable $\rho = \sqrt{\tau^2 + n^2}$ [24]. However, as mentioned in the introduction, in continuous media, LBs are unstable because small fluctuations in the intensity, beam size, or pulse width will lead to a phenomenon known as spatiotemporal collapse [5,24]. It is reasonable to expect that in the continuum limit [when the transverse size of LBs in the (n,τ) plane is large enough] broad LBs in WAs will have profiles similar to those of LBs found in continuous media. Indeed, in what follows we show the generation of broad LBs by using the following initial condition at the WA input for simulating Eq. (3): $a_n(\tau,0) = b_0\text{sech}(n/4)\text{sech}(\tau/4)$, where the initial peak amplitude b_0 will be varied to investigate the LB generation. The input parameters are the central wavelength $\lambda_0 = 1.55$ μm and the time scale $T_0 = 50$ fs; thus the initial pulse duration at the FWHM level for amplitude is calculated to be T_{FWHM} 525 fs. With these input parameters, the dispersion length (also the length scale here) is calculated to be $L_D = 10.07$ cm and the power scale $P_0 = 10.914$ kW. It is also helpful to compare the power scale P_0 with the critical power $P_{\text{cr}} = 3.77\lambda_0^2/8\pi n_0 n_2 \simeq 9.6$ MW for self-focusing of a Gaussian beam in fused silica at the central wavelength λ_0 [44], where n_0 and n_2 are the linear and nonlinear refractive indices of fused silica at λ_0, respectively. The input pulse covers 12 waveguides at the FWHM level. The total number of waveguides used here is $N = 141$. The evolution of the pulse is illustrated in Fig. 2(a) in the (n,τ,ξ) space for the initial peak amplitude $b_0 = 0.302$. The first and last frames in Fig. 2(a) are shown in Figs. 2(c) and 2(d), respectively, in the (n,τ) plane.

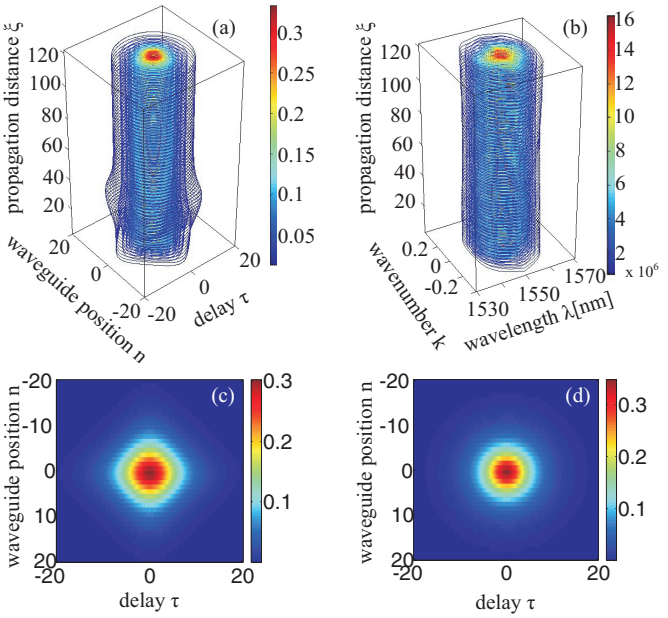

FIG. 2. (Color online) (a,b) Generation of a broad light bullet in the (n,τ,ξ) and (k,λ,ξ) spaces, respectively, when $b_0 = 0.302$. The first and last frames in (a) are shown in (c) and (d), respectively, in the (n,τ) plane.

As shown in Fig. 2(a), at the initial stage the profile of the pulse is adjusted, then after reaching the propagation distance $\xi \simeq 45$ the pulse profile becomes very stable, and the pulse now propagates like a LB without any significant distortion in profile and amplitude. As clearly shown in Fig. 2(c), the initial transversal profile of the pulse is reminiscent of a square, in particular in the periphery where amplitudes are weak. However, at the final frame [see Fig. 2(d)], like LBs in continuous media [24], the established profile of the LB looks like a perfect circle and only depends on the variable ρ. Note that for parameters used in Fig. 2 the factor $\eta = 1$ and we get the LB with circular profiles. If $\eta \neq 1$, one will get LBs with oval profiles. Note that in physical units the peak amplitude (around 0.3 in dimensionless units) in Fig. 2(a) will correspond to the peak power around $0.09P_0 \simeq 1$ kW, and the time scale $T_0 = 50$ fs as mentioned above.

Now if we take the Fourier transform $a(n,\tau,\xi) \to \tilde{a}(k,\lambda,\xi)$ (time domain τ and space domain n are transformed into wavelength domain λ and transverse wave-number domain k, respectively), then from Fig. 2(a) we obtain Fig. 2(b), which shows the LB evolution in the (k,λ,ξ) space. As shown in Fig. 2(b), the profile of the established LB in frequency domains k and λ is also stable during propagation. Note that,

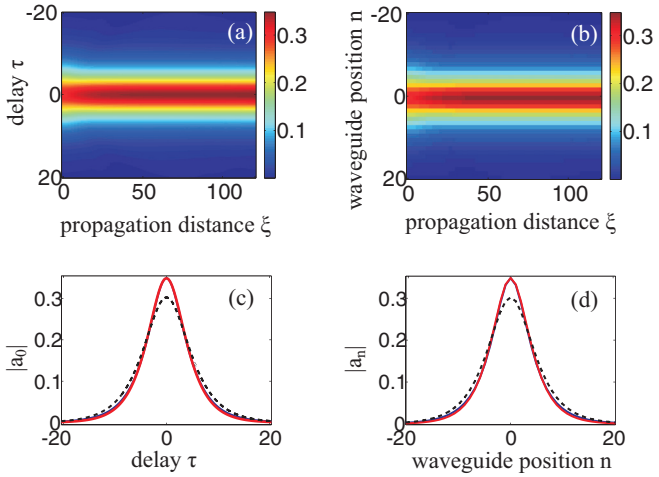

FIG. 3. (Color online) (a,b) Pulse propagation in the central waveguide $n = 0$ and with the delay $\tau = 0$, respectively. (c,d) The dashed black curves represent the input signal with the sech profile; solid blue curves represent the output profiles; solid red curves represent the curves fitted by the sech function, which are practically on top of the solid blue curves.

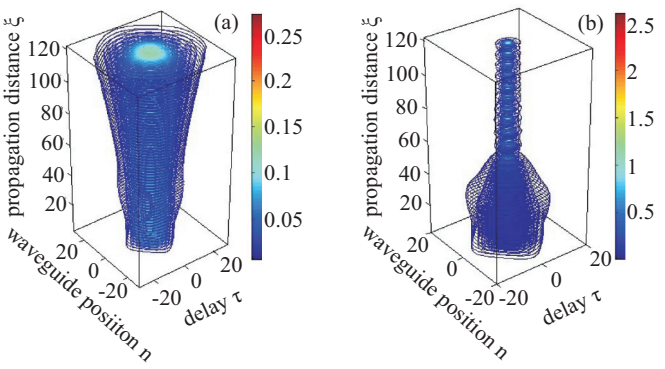

FIG. 4. (Color online) (a,b) Evolution of a pulse in the (n,τ,ξ) space when $b_0 = 0.28$ and 0.32, respectively.

although the initial profile of the pulse launched into WAs is not exactly the one for a LB, during propagation the pulse will nevertheless adjust its profile toward that of a LB. This feature shows that broad LBs in WAs form spontaneously and are quite robust.

We now analyze two special sections of Fig. 2(a) along the ξ axis. The section for the central waveguide ($n = 0$) is shown in Fig. 3(a), whereas the section for the central delay ($\tau = 0$) is shown in Fig. 3(b). The common feature of pulse evolution in Figs. 3(a) and 3(b) is that at the beginning the pulse is slightly compressed in both delay domain τ and space domain n, and then from a propagation distance of about $\xi \simeq 45$ the established profile of the LB is very stable. Note also that due to the discreteness of the space variable n details in Fig. 3(b) are rougher than in Fig. 3(a). The dashed (black) curves in Figs. 3(c) and 3(d) represent the input signal with sech profiles in Figs. 3(a) and 3(b), respectively. Meanwhile, the solid blue curves in Figs. 3(c) and 3(d) represent the output profiles in Figs. 3(a) and 3(b), respectively. The solid red curves in Figs. 3(c) and 3(d) represent the curves fitted by sech functions $a_0(\tau) = 0.3483\text{sech}(0.303\tau)$ and $a_n = 0.3483\text{sech}(0.303n)$, respectively. These fitted curves (red) are so similar to the calculated output profiles (blue) that they are almost on top of each other and one can only see extremely small differences between these curves at weak amplitudes ($a_{0,n} < 0.08$) by enlarging Figs. 3(c) and 3(d). So, in the case $\eta = 1$, due to the circular profile of the LB shown in Fig. 2(d) as discussed above, the LB profile can be well approximated by the sech function, which has only one variable $\rho = \sqrt{\tau^2 + n^2}$ as follows: $a(\rho) = 0.3483\text{sech}(0.303\rho)$. It is worth emphasizing that, for broad LBs, these fitted parameters inside (0.303) and outside (0.3483) the sech function comprise only one specific set of parameters among many others. Note also that the well-known fundamental temporal soliton in a single fiber has the profile $u(\tau) = q\text{sech}(q\tau)$ with the same factor q inside and outside the sech function [41].

In Figs. 2 and 3 we use the initial profile $a_n(\tau,0) = b_0\text{sech}(n/4)\text{sech}(\tau/4)$ with $b_0 = 0.302$ and, as a result, a broad LB is generated during propagation. If we now launch a pulse into WAs with lower initial peak amplitudes, it is reasonable to expect that in this case the diffraction-based broadening prevails over the nonlinearity-based focusing and pulses will spread out in both time and space. Indeed, this is the case as shown in Fig. 4(a) with $b_0 = 0.28$. In contrast, if initial peak amplitudes are higher, then one can expect the focusing in both space and time during propagation. This is demonstrated in Fig. 4(b) with $b_0 = 0.32$. After the first maximum compression in space and time at $\xi \simeq 54$ (where the energy of the pulse is practically localized only in the central waveguide) the pulse spreads out again, then gets compressed, and that periodic breathing of the pulse repeats again and again. However, as clearly shown in Fig. 4(b), during this periodic propagation the pulse is much localized as compared to the input pulse such that at its maximum broadening the pulse now only covers three waveguides at the FWHM level (compared to 12 at the input). Of course, the closer the initial peak amplitude to the value $b_0 = 0.302$ the better the pulse will conserve its shape during propagation, like the LB shown in Figs. 2 and 3.

Figures 5(a) and 5(b) show the evolution of pulses in the (n,τ,ξ) space when we increase further the initial peak amplitude of the pulse to the value $b_0 = 0.56$ and 0.84, respectively. The last frame in Figs. 5(a) and 5(b) is shown in Figs. 5(c) and 5(d), respectively, in the (n,τ) plane. As shown in Figs. 5(a) and 5(c) (when $b_0 = 0.56$) the initial pulse is split in time into three pulses: two intense compressed pulses which are symmetric with respect to the central delay $\tau = 0$ and a weaker and broader pulse in the center around $\tau = 0$. All three pulses are spatially symmetric with respect to the central waveguide with position $n = 0$. The two intense compressed pulses are extremely localized in both space and time where their peak amplitudes in the last frame shown in Fig. 5(c) are 2.58, 0.297, and 0.082 for waveguides with position $n = 0$, 1, and 2, respectively. These two intense pulses with narrow states are quite robust during propagation and have profiles similar to self-trapped LBs in WAs reported in [26]. So, when $b_0 = 0.56$ the initial pulse has enough energy to form only two narrow LBs in leading and trailing tails, and the residue of its energy forms a weak pulse around the central delay $\tau = 0$. If we increase the initial peak amplitude further up to the

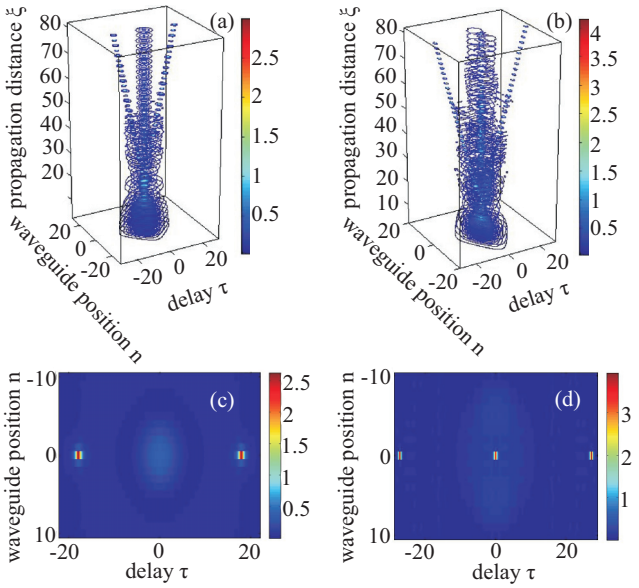

FIG. 5. (Color online) (a,b) Evolution of a pulse in the (n,τ,ξ) space when $b_0 = 0.56$ and 0.84, respectively.

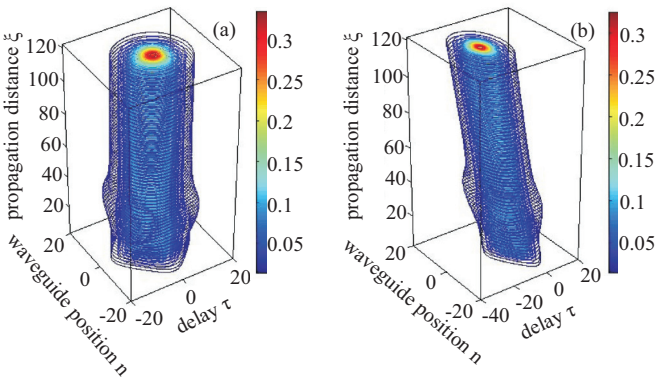

FIG. 6. (Color online) (a,b) Evolution of a broad light bullet in the (n,τ,ξ) space when the Raman effect and coupling dispersion are considered, respectively. The initial peak amplitude $b_0 = 0.302$ and 0.3 in (a) and (b), respectively. All other parameters are the same as in Fig. 2.

value $b_0 = 0.84$ [see Figs. 5(b) and 5(d)], the initial pulse will have enough energy to form three self-trapped LBs which are also symmetric with respect to the central delay $\tau = 0$. In this case three LBs are localized even more strongly than those in Figs. 5(a) and 5(c). Indeed, in the last frame shown in Fig. 5(d) the peak amplitudes of three LBs are 3.608, 0.1174, and 0.04 for waveguides with position $n = 0$, 1, and 2, respectively. Therefore, in this case one can say that almost all the energy of LBs is localized only in the central waveguide with position $n = 0$.

IV. INFLUENCE OF DISTURBING FACTORS ON THE GENERATION AND DYNAMICS OF LIGHT BULLETS

In the previous section we analyzed the generation and dynamics of broad LBs in a simplified model in the absence of several disturbing factors such as the Raman effect, HOD, and the coupling dispersion. All these effects play important roles in pulses' dynamics, in particular for short pulses having their durations in the femtosecond range [41]. However, as mentioned above, these factors are often neglected without any justification in investigating LBs in WAs. In this section we analyze the influence of these disturbing factors on the generation and dynamics of LBs in WAs made of silica. In order to do that, one needs to use the full model with Eq. (2) instead of the simplified model with Eq. (3). We first study the influence of the Raman effect without considering HOD and the coupling dispersion. It is well known that the strength of the Raman effect is inversely proportional to T_p^4, where T_p is the pulse duration at the moment of interest [45]. As reported in [46], even for a pulse with shorter initial duration ($T_{\mathrm{FWHM}} = 262$ fs) than that used in this work, the Raman effect plays a crucial role in pulse dynamics only right after the maximum compression of the pulse in the time domain and the simultaneous maximum broadening in the frequency domain, but the Raman effect plays a negligible role in pulse dynamics at the very beginning of the pulse propagation when the significant temporal compression has not taken place yet. So, one can expect that for the LB shown in Fig. 2 the Raman effect is not important. Indeed, this is the case, as shown in Fig. 6(a), where every condition and parameter is the same as in Fig. 2 with the only exception that now the Raman effect is considered in obtaining Fig. 6(a). By comparing Figs. 2(a) and 6(a) one can hardly see any visible differences. Actually, due to the Raman effect the LB is very slightly inclined in the time domain; thus now the LB center in the last frame in Fig. 6(a) is at $\tau_c = 0.7$ as compared to $\tau_c = 0$ in Fig. 2(d). Our simulations also reveal that HOD does not play a significant role for the LB shown in Fig. 2. Indeed, if we only consider HOD and ignore all other disturbing factors, then the LB shown in Fig. 2 will be only very slightly inclined in the time domain; thus the LB center in the last frame will now be at $\tau_c = 0.2$ (not shown here) as compared to $\tau_c = 0$ in Fig. 2(d). This is understandable, because as shown in Fig. 2(b) the spectrum of this LB is fairly narrow, with the outer contour in Fig. 2(b) being spanned from 1540–1560 nm where the dispersion parameter D shown in Fig. 1 is only varied in the range $19 < D < 20$ in its conventional unit [ps/(nm km)]; thus D changes about 5%. In this specific case, one can ignore the Raman and HOD effects in the dynamics of the LB in Fig. 2. However, the influence of the coupling dispersion on the dynamics of the LB shown in Fig. 2 is more noticeable with specific parameters used in this work. With parameters used in this work, in the wavelength interval 1540–1560 nm the coupling coefficient is varied in the range $0.0046 < \kappa < 0.0053$ mm^{-1}; thus κ changes about 14%. Figure 6(b) shows the LB dynamics where every condition and parameter is the same as in Fig. 2 with only two exceptions that now the coupling dispersion is considered and the initial peak amplitude $b_0 = 0.3$ is used in Fig. 6(b) instead of the value 0.302 in Fig. 2. As clearly shown in Fig. 6(b), the LB is now significantly inclined in the time domain and the LB center in the last frame in Fig. 6(b) is at $\tau_c = -18.5$. With the initial peak amplitude $b_0 = 0.3$ used in Fig. 6(b) the LB is formed during propagation. If $b_0 = 0.302$ is used, then the only difference with the current Fig. 6(b) is that after

reaching the propagation distance $\xi \simeq 50$ the spatiotemporal pulse in Fig. 6(b) will be slightly and gradually compressed (not shown here) in both time and space domains. Therefore, here we can make a local conclusion that the broad light bullet shown in Fig. 2 is robust and can retain its shape for long propagation distances even in the presence of disturbing factors such as the Raman effect, HOD, and coupling dispersion. This is expected because these disturbing factors are crucial only when the spectra become wide enough (e.g., due to the strong temporal compression as shown below). For the LB in Fig. 2 the temporal compression, and thus the spectral broadening, almost do not take place during propagation. As a result, the above-mentioned disturbing factors are not strong enough to break the establishment of the LB during propagation. In addition, our simulations (not shown here) with input conditions being the right profile of broad LBs taken from Fig. 2(d) and superposed with some random weak noise show that broad LBs are not destroyed by weak noise. This feature also indicates that broad LBs in WAs are robust.

However, the disturbing factors will be crucial if the significant temporal compression of the pulse takes place during propagation. This is dramatically demonstrated in Fig. 7 when the pulse and parameters in Fig. 4(b) with $b_0 = 0.32$ are used, but now in the presence of the Raman effect. Figure 7(a) shows the pulse propagation in the (n,τ,ξ) space, whereas the pulse propagation in the central waveguide (with position $n = 0$) is shown in Fig. 7(b). Note that, although the step along the ξ axis in simulations is small enough, due to a huge amount of data obtained during simulations for getting Figs. 7(a) and 7(b) we are able to pick only 60 frames along the ξ axis to show the result. Figures 7(c) and 7(d) show the pulse profile at the final frame in Fig. 7(a) at the central waveguide and at the delay $\tau = 18.37$, respectively. In Figs. 7(c) and 7(d) the dashed (blue) curves are the results obtained through direct pulse propagation simulation, whereas the solid (red) curves are fitted with sech functions. At the beginning of the propagation ($\xi < 50$) the pulse is only slightly compressed in time and space; thus the disturbing factors do not play big roles in the pulse dynamics. As a result, at this stage the pulse dynamics in Figs. 4(b) and 7(a) are almost the same. However, at longer distances, its temporal compression is very strong, and thus its spectral broadening is enhanced enough to make all disturbing factors important now. After the maximum spatiotemporal compression at $\xi \simeq 54$, the dynamics of the pulse in Fig. 7(a) (where the Raman effect is included) is totally different from that shown in Fig. 4(b) (where the Raman effect is excluded). In the latter case [see Fig. 4(b)] the pulse breathing takes place in both space (in the n axis) and time, and the pulse center (at $\tau = 0$) does not change during propagation. However, in Fig. 7(a) most of the energy of the pulse is trapped in the central waveguide with position $n = 0$ and two neighboring waveguides with indices $n = 1, -1$ [see Fig. 7(d)]. In the time domain, due to the Raman effect the trapped pulse is also strongly compressed and bent toward the trailing tail ($\tau > 0$) [see Fig. 7(b)]. Note that after reaching the bottom part in the time window used in simulations [see the white arrow at $\tau \simeq +40$ in Fig. 7(b)], physically, the pulse will be bent further to the trailing tail ($\tau > 0$); however, visually, it will emerge at the top part of the time window [see the white arrow at $\tau \simeq -40$ in Fig. 7(b)]. This

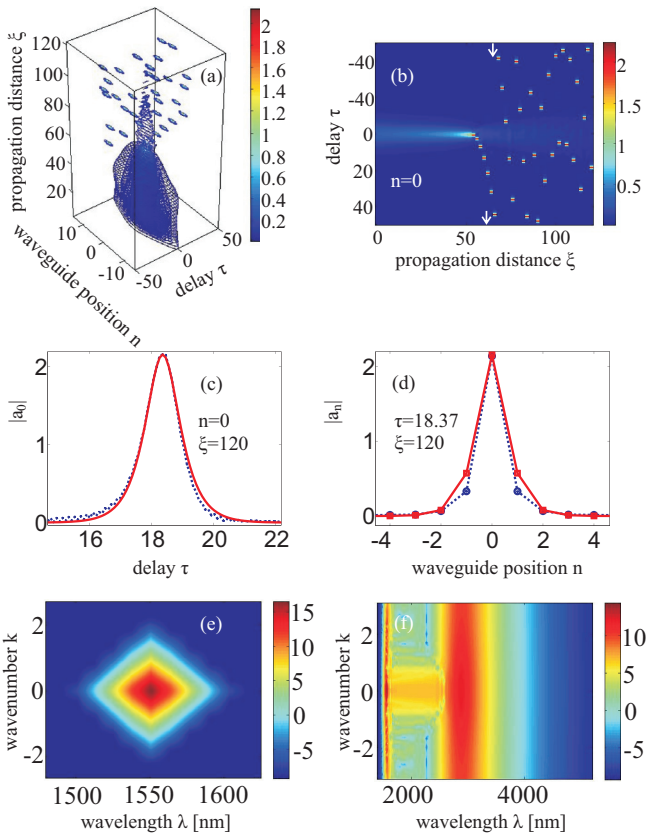

FIG. 7. (Color online) (a,b) Evolution of a pulse with Raman effect and $b_0 = 0.32$ in the (n,τ,ξ) space and in the (τ,ξ) plane for the central waveguide ($n = 0$), respectively. (c,d) The pulse profile at the final frame in (a) at the central waveguide and at the delay $\tau = 18.37$, respectively. The dashed (blue) curves in (c,d) are the results obtained through direct pulse propagation simulation, whereas the solid (red) curves are fitted with sech functions. The first and last frames in (a) are shown in (e) and (f), respectively, in the (k,λ) plane and on a logarithmic scale.

feature is common in the split-step Fourier technique and the accuracy of simulations is not influenced by the width of the time window. It is worth mentioning that after the generation of the trapped pulse its width in time and space (in the n axis) is conserved during propagation, and as demonstrated in Figs. 7(a) and 7(b) this trapped light bullet is very robust. Due to the Raman effect, the pulse profile in the time domain is now slightly asymmetric [see the dashed (blue) curve in Fig. 7(c)]. In Figs. 7(e) and 7(f) we plot the contour plots of the first and last frames in Fig. 7(a), but now in the (k,λ) plane and on a logarithmic scale. The spectral broadening and Raman-based redshift are evident from Figs. 7(e) and 7(f). Note that although the energy of the pulse is strongly localized in Figs. 5 and 7 the maximum peak intensity in these figures is roughly estimated to be $16P_0/\pi r^2 \simeq 1.6 \times 10^{11}$ W/cm^2 (with $r = 6$ μm being the core radius used in this work), which is well below the intensity threshold $I_{cr} \simeq 10^{13}$ W/cm^2 for bulk optical breakdown of transparent solids using a femtosecond laser pulse [47]. Therefore, in this work we can safely neglect the plasma generation effect.

We would like to stress that the results shown in Fig. 7 are obtained when the Raman effect is included, but HOD and the coupling dispersion are excluded. If all these factors are included, then after the maximum temporal compression one can obtain the supercontinuum generation in both wavenumber and frequency domains (see [23] for more details). In this case, it will be more difficult to generate narrow LBs. Thus, one needs to carefully optimize parameters of WAs and input pulse such that HOD and coupling dispersion are less pronounced, and as a result narrow LBs can be generated. Note that, unlike narrow LBs, as mentioned above, broad LBs shown in Fig. 2 still can be easily formed and conserve their shape for long propagation distances even under the combined influence of all these disturbing factors.

V. CONCLUSIONS

In conclusion, we have demonstrated with accurate numerical simulations that broad LBs can be established during propagation of pulses which are slightly different from LBs at the input of waveguide arrays made of material with Kerr-type nonlinearity. These broad LBs can be analytically constructed with a high degree of accuracy by using the hyperbolic secant function. The discrete nature of waveguide arrays helps arrest the collapse of these LBs even in the presence of the Raman effect, coupling dispersion, and high-order dispersion. However, these broad LBs are only metastable as compared to narrow LBs whose energy is almost located in three adjacent waveguides. These narrow LBs are extremely robust even in the presence of the Raman effect and can be generated from initial pulses whose profiles are too different from established ones of narrow LBs. We expect that LBs will find various applications in science and technology in the future.

ACKNOWLEDGMENTS

F.B. (Max Planck Research Group) and T.X.T. (Max Planck Partner Group) are supported by the German Max Planck Society for the Advancement of Science.

[1] D. N. Christodoulides, F. Lederer, and Y. Silberberg, Nature (London) **424**, 817 (2003).
[2] A. L. Jones, J. Opt. Soc. Am. **55**, 261 (1965).
[3] J. W. Fleischer, M. Segev, N. K. Efremidis, and D. N. Christodoulides, Nature (London) **422**, 147 (2003).
[4] D. N. Christodoulides and R. I. Joseph, Opt. Lett. **13**, 794 (1988).
[5] Y. S. Kivshar and G. P. Agrawal, *Optical Solitons: From Fiber to Photonic Crystals*, 5th ed. (Academic, New York, 2003).
[6] G. P. Agrawal, *Applications of Nonlinear Fiber Optics*, 2nd ed. (Academic, New York, 2008).
[7] M. Bellec, P. Panagiotopoulos, D. G. Papazoglou, N. K. Efremidis, A. Couairon, and S. Tzortzakis, Phys. Rev. Lett. **109**, 113905 (2012).
[8] U. Peschel, T. Pertsch, and F. Lederer, Opt. Lett. **23**, 1701 (1998).
[9] T. Pertsch, P. Dannberg, W. Elflein, A. Bräuer, and F. Lederer, Phys. Rev. Lett. **83**, 4752 (1999).
[10] G. Lenz, I. Talanina, and C. M. de Sterke, Phys. Rev. Lett. **83**, 963 (1999).
[11] F. Lederer, G. I. Stegeman, D. N. Christodoulides, G. Assanto, M. Segev, and Y. Silberberg, Phys. Reports **463**, 1 (2008).
[12] D. N. Christodoulides and E. D. Eugenieva, Phys. Rev. Lett. **87**, 233901 (2001).
[13] S. Longhi, Opt. Lett. **35**, 235 (2010).
[14] F. Dreisow, R. Keil, A. Tünnermann, S. Nolte, S. Longhi, and A. Szameit, Europhys. Lett. **97**, 10008 (2012).
[15] S. Longhi, Appl. Phys. B **104**, 453 (2011).
[16] J. M. Zeuner, N. K. Efremidis, R. Keil, F. Dreisow, D. N. Christodoulides, A. Tünnermann, S. Nolte, and A. Szameit, Phys. Rev. Lett. **109**, 023602 (2012).
[17] Tr. X. Tran, S. Longhi, and F. Biancalana, Ann. Phys. **340**, 179 (2014).
[18] Tr. X. Tran, X. N. Nguyen, and D. C. Duong, J. Opt. Soc. Am. B **31**, 1132 (2014).
[19] Tr. X. Tran and F. Biancalana, Phys. Rev. Lett. **110**, 113903 (2013).
[20] N. Akhmediev and M. Karlsson, Phys. Rev. A **51**, 2602 (1995).
[21] F. Biancalana, D. V. Skryabin, and A. V. Yulin, Phys. Rev. E **70**, 016615 (2004).
[22] Tr. X. Tran and F. Biancalana, Opt. Exp. **21**, 17539 (2013).
[23] Tr. X. Tran, D. C. Duong, and F. Biancalana, Phys. Rev. A **89**, 013826 (2014).
[24] Y. Silberberg, Opt. Lett. **15**, 1282 (1990).
[25] B. A. Malomed, D. Mihalache, F. Wise, and L. Torner, J. Opt. B: Quantum Semiclass. Opt. **7**, R53 (2005).
[26] A. B. Aceves, C. De Angelis, A. M. Rubenchik, and S. K. Turitsyn, Opt. Lett. **19**, 329 (1994).
[27] A. B. Aceves, G. G. Luther, C. De Angelis, A. M. Rubenchik, and S. K. Turitsyn, Phys. Rev. Lett. **75**, 73 (1995).
[28] A. B. Aceves, G. G. Luther, C. De Angelis, A. M. Rubenchik, and S. K. Turitsyn, Opt. Fiber Technol. **1**, 244 (1995).
[29] E. W. Laedke, K. H. Spatschek, S. K. Turitsyn, and V. K. Mezentsev, Phys. Rev. E **52**, 5549 (1995).
[30] A. V. Buryak and N. N. Akhmediev, IEEE J. Quantum Electron. **31**, 682 (1995).
[31] A. B. Aceves, M. Santagiustina, and C. De Angelis, J. Opt. Soc. Am. B **14**, 1807 (1997).
[32] X. Liu, L. J. Qian, and F. W. Wise, Phys. Rev. Lett. **82**, 4631 (1999).
[33] H. S. Eisenberg, R. Morandotti, Y. Silberberg, S. Bar-Ad, D. Ross, and J. S. Aitchison, Phys. Rev. Lett. **87**, 043902 (2001).
[34] D. Cheskis, S. Bar-Ad, R. Morandotti, J. S. Aitchison, H. S. Eisenberg, Y. Silberberg, and D. Ross, Phys. Rev. Lett. **91**, 223901 (2003).
[35] C. J. Benton, A. V. Gorbach, and D. V. Skryabin, Phys. Rev. A **78**, 033818 (2008).
[36] N. N. Rosanov, *Spatial Hysteresis and Optical Patterns* (Springer, New York, 2002).
[37] N. N. Rosanov, in *Dissipative Solitons*, edited by N. Akhmediev and A. Ankiewicz (Springer-Verlag, New York, 2005).
[38] P. Grelu, J. M. Soto-Crespo, and N. Akhmediev, Opt. Exp. **13**, 9352 (2005).

[39] P. Panagiotopoulos, A. Couairon, N. K. Efremidis, D. G. Papazoglou, and S. Tzortzakis, Opt. Express **19**, 10057 (2011).
[40] D. N. Neshev, A. A. Sukhorukov, A. Dreischuh, R. Fischer, S. Ha, J. Bolger, L. Bui, W. Krolikowski, B. J. Eggleton, A. Mitchell, M. W. Austin, and Y. S. Kivshar, Phys. Rev. Lett. **99**, 123901 (2007).
[41] G. P. Agrawal, *Nonlinear Fiber Optics*, 5th ed. (Academic, New York, 2013).
[42] A. Szameit, D. Blömer, J. Burghoff, T. Pertsch, S. Nolte, and A. Tünnermann, Appl. Phys. B **82**, 507 (2006).
[43] R. Tewari and K. Thyagarajan, J. Lightwave Technol. **4**, 386 (1986).
[44] J. H. Marburger, Prog. Quantum Electron. **4**, 35 (1975).
[45] J. P. Gordon, Opt. Lett. **11**, 662 (1986).
[46] Tr. X. Tran and F. Biancalana, Phys. Rev. A **79**, 065802 (2009).
[47] C. B. Schaffer, A. Brodeur, J. F. Garcia, and E. Mazur, Opt. Lett. **26**, 93 (2001).